Mon. Not. R. Astron. Soc. **000**, 000–000 (0000) Printed 12 September 2006 (MN LATEX style file v2.2)

Boltzmann moment equation approach for the numerical study of anisotropic stellar disks

E. I. Vorobyov[1⋆] and Ch. Theis[2]
[1] *CITA National Fellow, Department of Physics and Astronomy, University of Western Ontario, London, Ontario, N6A 3K7, Canada.*
[2] *Institut für Astronomie, Universität Wien, Türkenschanzstr. 17, 1180 Wien, Austria.*

to appear MNRAS

ABSTRACT

We present the Boltzmann moment equation approach for the dynamics of stars (BEADS-2D), which is a finite-difference Eulerian numerical code designed for the modelling of *anisotropic and non-axisymmetric* flat stellar disks. The BEADS-2D code solves the Boltzmann moment equations up to second order in the thin-disk approximation. This allows us to obtain the anisotropy of the velocity ellipsoid and the vertex deviation in the plane of the disk.

We study the time-dependent evolution of exponential stellar disks in the linear regime and *beyond*. The disks are initially characterized by different values of the Toomre parameter $Q_{\rm s}$ and are embedded in a dark matter halo, yielding a rotation curve composed of a rigid central part and a flat outer region. Starting from a near equilibrium state, several unstable modes develop in the disk. In the early linear phase, the very centre and the large scales are characterized by growing one-armed and bisymmetric positive density perturbations, respectively. This is in agreement with expectations from the swing amplification mechanism of short-wavelength trailing disturbances, propagating through the disk centre. In the late linear phase, the overall appearance is dominated by a two-armed spiral structure localized within the outer Lindblad resonance (OLR). During the non-linear evolutionary phase, radial mass redistribution due to the gravitational torques of spiral arms produces an outflow of mass, which forms a ring at the OLR, and an inflow of mass, which forms a transient central bar. This process of mass redistribution is self-regulatory and it terminates when spiral arms diminish due to a shortage of matter. Finally, a compact central disk and a diffuse ring at the OLR are formed. An increase in $Q_{\rm s}$ stabilizes the disks at $Q_{\rm s} \approx 3.15$, in agreement with the theoretical predictions.

Considerable vertex deviations are found in regions with strongly perturbed mass distributions, i.e. near the spiral arms. The vertex deviations are especially large at the convex edge of the spiral arms, whereas they are small at the concave edge. The mean vertex deviations correlate well with the global Fourier amplitudes, reaching mean values of about 12° in the saturation stage. Local values of the vertex deviation can reach up to almost 90°. Near the convex edge of the spiral arms, the ratio of radial to azimuthal components of the velocity ellipsoid can deviate considerably from the values predicted from the epicycle approximation.

Key words: Galaxies: general – galaxies: evolution – galaxies: spiral – galaxies: kinematics and dynamics

1 INTRODUCTION

The majority of normal disk galaxies are characterized by non-axisymmetric structures like spirals or bars. These structural elements have been widely discussed in the literature as a result of gravitational instabilities which are connected to growing density waves or global instabilities of disks (e.g. Binney & Tremaine 1987, afterwards BT87).

A first insight into the properties of galactic discs was provided by linear stability analysis. Structure growth in a stellar disk within the linear regime was studied via the lin-

⋆ E-mail: vorobyov@astro.uwo.ca (EIV); theis@astro.univie.ac.at (ChT)

earised collisionless Boltzmann equation by Toomre (1964), Zang (1976), Pichon & Cannon (1997), Evans & Read (1998), Jalali & Hunter (2005), and others. Toomre (1964) has deduced a simple stability criterion from the Jeans equations in case of stellar disks: a stellar disk is stable against axisymmetric perturbations if $Q_{\rm s} \equiv \sigma_{rr}\kappa/(3.36G\Sigma)$ exceeds a critical value $Q_{\rm s,crit} = 1$ (σ_{rr} is the radial velocity dispersion, κ is the epicycle frequency, G is the gravitational constant, and Σ is the surface density of the disk). In case of non-axisymmetric perturbations the analysis becomes technically more difficult, but the Toomre parameter turned out to still be a good indicator for stability, if one increases its critical value (Bertin et al. 1989, Polyachenko et al. 1997).

A disadvantage of linear stability analysis is its restriction to small perturbations, both in amplitude and wavelength. Once the perturbations exceed a critical level or when the initial perturbations are already large, numerical simulations are necessary. Hydrodynamical simulations revealed three qualitatively distinct phases for the growth of unstable disks (Laughlin et al. 1997). Starting from small amplitudes, perturbations grow first linearly. When they reach a critical level, mode-mode coupling becomes important and the non-linear evolution starts. The self-interaction of the dominant mode might result in a rearrangement of the radial mass distribution ($m = 0$ mode). The disk itself might become violently unstable, which is indicated by the perturbations reaching a "macroscopic" level. Finally, a quasi-equilibrium saturation stage can be reached when the growth of the instabilities is stopped due to shocks or feedback mechanisms heating up the disk dynamically. Otherwise, fragmentation continues until the disk is destroyed or transformed.

Though N-body simulations have been proven to be extremely useful for many studies of galactic dynamics, they are less suitable for studying the growth of very weak perturbations. The main reason is that N-body calculations of galaxies are usually performed with less particles than the actual number of stars in these systems. This causes an inherent artificial particle noise which cannot be neglected for typical particle numbers.

Alternatively, numerical hydrodynamics simulations became a primary tool for the analysis of growing spiral instabilities (e.g. Korchagin et al. 2000, Orlova et al. 2002). First, they allow for a direct comparison with the results of a semi-analytic linear stability analysis, including predictions for the growth rates (Laughlin et al. 1997; 1998, Korchagin et al. 2000), because the same set of basic equations is applied. Second, the standard grid methods used to solve the hydrodynamical equations allow to start with very small perturbations (basically limited by machine accuracy). Their evolution can be followed over many e-folding times until they reach the non-linear regime and beyond.

A major drawback of purely hydrodynamical simulations is that the dominant disk component is the stellar disk. The latter is characterized by an *anisotropic velocity dispersion*, whereas the hydrodynamical equations deal with an *isotropic pressure*. Secondly, one has to assume an equation of state connecting pressure, (surface) density and temperature (velocity dispersion). For instance, if one assumes a polytropic-like equation of state, i.e. $P = C\,\Sigma^{\gamma}$, the set of hydrodynamic equations is closed with the Euler equation describing the momentum transport (for an example of a stability analysis based on such assumptions see e.g. Aoki et al. 1979). Since the temperature does not show up in the polytropic equation of state, no energy transport equation is required. Obviously, this is a convenient simplification which, however, might not be generally applicable. Moreover, the profile of the Toomre parameter is completely fixed by the surface density distribution.

A more complete ansatz for describing stellar disks is the collisionless Boltzmann equation (BT87)

$$\frac{\partial f}{\partial t} + \boldsymbol{v}\cdot\frac{\partial f}{\partial \boldsymbol{r}} + \dot{\boldsymbol{v}}\cdot\frac{\partial f}{\partial \boldsymbol{v}} = 0, \qquad (1)$$

where $f(\boldsymbol{r},\boldsymbol{v},t)$ is the distribution function. The term $\dot{\boldsymbol{v}}$ includes accelerations like gravitational forces, pressure terms, etc. Since a direct solution is already numerically very difficult, the problem is often reduced by taking the velocity moments of equation (1). By this, one gets an infinite series of moment equations where the equations for moment i include moments of the order $i+1$. The knowledge of all velocity moments is equal to the knowledge of the distribution function itself. Practically, one has to terminate the set of equations by a closure condition. Setting all moments of third order to zero (zero-heat-flux condition) results in the Jeans equations which are well applicable to stellar systems with negligible two-body relaxation. In that case, the second order moment equations which yield information on the velocity ellipsoid are included and stellar anisotropy can be considered. An example are the one- and two-dimensional chemo-dynamical models by Theis et al. (1992) and Samland et al. (1997). For the special case of galactic disks, Amendt & Cuddeford (1991) and Cuddeford & Amendt (1991) studied the higher order moments in detail. They found that for reasonable constraints to the distribution function the third order terms vanish to leading order in the plane of the disk. This corroborates the assumption of a zero-heat-flux. Extensions of the Boltzmann moment equations including collisional processes have also been used (e.g. Larson 1970, Louis 1990 or Giersz & Spurzem 1994 for the evolution of star clusters).

In this paper we present the Boltzmann equation approach for the dynamics of stars (BEADS-2D), which is a numerical code that solves the Boltzmann moment equations up to second order using the methods of finite-differences. The BEADS-2D code is applied to study the time-dependent evolution of flat, non-isotropic stellar disks in the linear regime and *beyond*. In contrast to previous numerical studies, we include the *non-axisymmetric* velocity dispersion terms into the Boltzmann moment equations. Therefore, our approach allows us to study the evolution of the anisotropy and the vertex deviation of the stellar component. We compare the stability properties of non-isotropic stellar disks with the predictions of linear stability analysis for non-isotropic disks by Polyachenko et al. (1997). We provide a physical interpretation for growing instabilities in our model stellar disks.

In the following section we describe the Boltzmann moment equation approach. The basic principles of the BEADS-2D code are discussed in § 3. The results of numerical modelling are presented in § 4. Finally, conclusions and a summary are given in § 5.

2 STELLAR SYSTEMS: THE MOMENT EQUATION APPROACH

2.1 The 3D-Boltzmann moment equations

Stars are collisionless objects that move on orbits determined by the large-scale gravitational potential Φ. An exact description of such a system requires the solution of the collisionless Boltzmann equation (1) for the distribution function of stars $f(\boldsymbol{r},\boldsymbol{v},t)$ in the phase space $(\boldsymbol{r},\boldsymbol{v})$. The distribution function of stars $f \equiv f(\boldsymbol{r},\boldsymbol{v},t)$ contains a fundamental description of the stellar system. Its lower order moments like the density $\rho = \int f\, d^3\boldsymbol{v}$, the mean velocity $\boldsymbol{u} = \rho^{-1} \int f\, \boldsymbol{v}\, d^3\boldsymbol{v}$, or the velocity-dispersion tensor $\sigma_{ij}^2 = \rho^{-1} \int f\,(v_i - u_i)(v_j - u_j)\, d^3\boldsymbol{v}$ of stars can be deduced – at least partly – from observations. The corresponding equations for ρ, $\rho\mathbf{u}$, and $\rho\sigma_{ij}^2$ can be obtained by taking moments of the collisionless Boltzmann equation (1). If one closes the system by assuming the zero-heat-flux approximation $Q_{ijk} = \rho^{-1} \int f\,(v_i - u_i)(v_j - u_j)(v_k - u_k)\, d^3\boldsymbol{v} = 0$, a set of ten partial differential equations (the velocity dispersion tensor is symmetric by definition) can be derived (see Appendix A).

The three off-diagonal elements of the velocity-dispersion tensor can be regarded as a measure of alignment of the principal axes of the velocity ellipsoid with respect to the coordinate system. We note that these terms may become both positive or negative (although they have a square mark), as follows directly from the definition of the velocity-dispersion tensor.

In our models, the gravitational potential Φ is composed of the sum of an external contribution $\Phi_{\rm ext}(\boldsymbol{r},t)$ and the self-gravity $\Phi_{\rm sys}(\boldsymbol{r},t)$ of the disk mass distribution $\rho(\boldsymbol{r})$ obeying the moment equations. Its potential can be derived from the Poisson equation

$$\Delta\Phi_{\rm sys} = 4\pi G\rho. \tag{2}$$

The external term describes any known (eventually time-dependent) potential like a dark matter halo, whereas the "system" corresponds to the live disk.

2.2 The 2D-Boltzmann moment equations for flat disks

A substantial fraction of stars in spiral galaxies are concentrated in the disk. Hence to a first approximation, stellar disks may be regarded as having zero thickness. In the thin-disk approximation, all motions are localized within the (r,ϕ) plane. The moment equations in the thin-disk approximation can be obtained from equations (A1)-(A10) by assuming a vanishing z-gradient of all physical variables and setting $u_z = 0$ (negligible vertical motion), $\sigma_{zr}^2 = 0$, and $\sigma_{\phi z}^2 = 0$. The stellar volume density ρ is vertically integrated to yield the surface density Σ. The assumptions of $\sigma_{zr}^2 = 0$, and $\sigma_{z\phi}^2 = 0$ are justified on observational grounds (Binney & Merrifield 1998). The vertical velocity dispersion σ_{zz} is obtained by assuming a constant ratio of the vertical to the radial (azimuthal) velocity dispersions. Below, we provide the moment equations in the thin-disk approximation written in polar coordinates. For the convenience of coding, the advection terms are set in brackets.

Continuity equation:

$$\frac{\partial\Sigma}{\partial t} + \left[\frac{1}{r}\frac{\partial}{\partial r}(r\cdot\Sigma\cdot u_r) + \frac{1}{r}\frac{\partial}{\partial\phi}(\Sigma\cdot u_\phi)\right] = 0. \tag{3}$$

Momentum equations:

$$\begin{aligned}\frac{\partial}{\partial t}(\Sigma u_r) &+ \left[\frac{1}{r}\frac{\partial}{\partial r}(r\cdot\Sigma u_r\cdot u_r) + \frac{1}{r}\frac{\partial}{\partial\phi}(\Sigma u_r\cdot u_\phi)\right]\\ &- \frac{\Sigma u_\phi^2}{r} + \frac{1}{r}\frac{\partial}{\partial r}(r\Sigma\sigma_{rr}^2) + \frac{1}{r}\frac{\partial}{\partial\phi}(\Sigma\sigma_{r\phi}^2)\\ &- \frac{\Sigma\sigma_{\phi\phi}^2}{r} + \Sigma\frac{\partial\Phi}{\partial r} = 0,\end{aligned} \tag{4}$$

$$\begin{aligned}\frac{\partial}{\partial t}(\Sigma r u_\phi) &+ \left[\frac{1}{r}\frac{\partial}{\partial r}(r\cdot\Sigma r u_\phi\cdot u_r) + \frac{1}{r}\frac{\partial}{\partial\phi}(r\Sigma u_\phi\cdot u_\phi)\right]\\ &+ r\left\{\frac{\partial}{\partial r}(\Sigma\sigma_{\phi r}^2) + \frac{1}{r}\frac{\partial}{\partial\phi}(\Sigma\sigma_{\phi\phi}^2) + \frac{2}{r}\Sigma\sigma_{r\phi}^2\right\}\\ &+ \Sigma\frac{\partial\Phi}{\partial\phi} = 0.\end{aligned} \tag{5}$$

Velocity dispersion equations:

$$\begin{aligned}\frac{\partial}{\partial t}(\Sigma\sigma_{rr}^2) &+ \left[\frac{1}{r}\frac{\partial}{\partial r}(r\cdot\Sigma\sigma_{rr}^2\cdot u_r) + \frac{1}{r}\frac{\partial}{\partial\phi}(\Sigma\sigma_{rr}^2\cdot u_\phi)\right]\\ &+ 2\Sigma\sigma_{r\phi}^2\left\{\frac{1}{r}\frac{\partial u_r}{\partial\phi} - \frac{2u_\phi}{r}\right\}\\ &+ 2\Sigma\sigma_{rr}^2\frac{\partial u_r}{\partial r} = 0,\end{aligned} \tag{6}$$

$$\begin{aligned}\frac{\partial}{\partial t}(\Sigma\sigma_{\phi\phi}^2) &+ \left[\frac{1}{r}\frac{\partial}{\partial r}(r\cdot\Sigma\sigma_{\phi\phi}^2\cdot u_r) + \frac{1}{r}\frac{\partial}{\partial\phi}(\Sigma\sigma_{\phi\phi}^2\cdot u_\phi)\right]\\ &+ 2\Sigma\sigma_{\phi\phi}^2\left\{\frac{u_r}{r} + \frac{1}{r}\frac{\partial u_\phi}{\partial\phi}\right\}\\ &+ 2\Sigma\sigma_{r\phi}^2\left\{\frac{u_\phi}{r} + \frac{\partial u_\phi}{\partial r}\right\} = 0,\end{aligned} \tag{7}$$

$$\begin{aligned}\frac{\partial}{\partial t}(\Sigma\sigma_{r\phi}^2) &+ \left[\frac{1}{r}\frac{\partial}{\partial r}(r\cdot\Sigma\sigma_{r\phi}^2\cdot u_r) + \frac{1}{r}\frac{\partial}{\partial\phi}(\Sigma\sigma_{r\phi}^2\cdot u_\phi)\right]\\ &+ \Sigma\sigma_{r\phi}^2\left\{\frac{1}{r}\frac{\partial}{\partial r}(ru_r) + \frac{1}{r}\frac{\partial u_\phi}{\partial\phi}\right\}\\ &+ \Sigma\sigma_{rr}^2\left\{\frac{u_\phi}{r} + \frac{\partial u_\phi}{\partial r}\right\}\\ &+ \Sigma\sigma_{\phi\phi}^2\left\{\frac{1}{r}\frac{\partial u_r}{\partial\phi} - \frac{2u_\phi}{r}\right\} = 0.\end{aligned} \tag{8}$$

According to our experience, equations (3)-(8) are expressed in the computationally most stable form. For convenience we will use the name *kinetic equations* or *kinetic models* when we solve the second order Boltzmann moment equations.

2.3 The gravitational potential

In our models the gravitational potential consists of two parts, a live disk and a static halo component. The gravitational potential $\Phi_{\rm disk}$ of the flat disk can be calculated by

(BT87, Sect. 2.8)

$$\Phi_{\rm disk}(r,\phi) = -G\int_0^\infty r'dr' \times \int_0^{2\pi} \frac{\Sigma(r',\phi')d\phi'}{\sqrt{r'^2+r^2-2rr'\cos(\phi'-\phi)}}. \quad (9)$$

This sum is calculated using a FFT technique which applies the 2D Fourier convolution theorem for polar coordinates.

The halo properties are fixed by the rotation curve parametrized by

$$v_{\rm c} = v_\infty \cdot \left(\frac{r}{r_{\rm flat}}\right) \cdot \frac{1}{\left[1+\left(\frac{r}{r_{\rm flat}}\right)^{n_v}\right]^{\frac{1}{n_v}}}. \quad (10)$$

The transition radius between an inner region of rigid rotation and a flat rotation in the outer part is given by $r_{\rm flat}$ which we set to 3 kpc. The smoothness of the transition is controlled by the parameter n_v, set to 2. The velocity at infinity, v_∞, was set to 208 km s^{-1}. The solid line in Fig. 1 shows the rotation curve we used. The corresponding halo potential $\Phi_{\rm halo}$ is then derived from equation (4), where Φ is substituted with $\Phi_{\rm halo}+\Phi_{\rm disk}$ and u_r is set to zero.

3 NUMERICAL MODELLING

3.1 The BEADS-2D code

The 2D-equations for thin disks are discretized on an Eulerian grid with a logarithmic grid spacing in the r-direction and uniform grid spacing in the ϕ-direction. The different terms are taken into account by applying an operator splitting technique similar to the ZEUS program (Stone & Norman 1992). Advection is performed by the second-order van-Leer scheme. The time step is determined according to the usual Courant-Friedrichs-Levy criterion modified to take into account the velocity dispersion. Namely, we diagonalize the velocity dispersion tensor at each time step and use the diagonal components in the time-step limiter. For our simulations we use reflecting boundary conditions in the radial direction (and periodic boundary conditions in the azimuthal direction). Our simulations are done on a grid with 256×256 cells covering the radial range from 0.2 kpc to 30-45 kpc (depending on the model). The gravitational force of a thin disk near its inner boundary at $r = 0.2$ kpc is directed radially outward, which is an artificial effect due to the lack of material within the inner boundary (note that such a problem would not exist in the case of spherical symmetry). In order to reduce the magnitude of this spurious outward gravity force, we introduce an inner circular disk of constant density and outer radius $r_{\rm out} = 0.2$ kpc. This inner disk merely serves as a central gravity source and its gravitational potential $\Phi_{\rm id}$ can be computed by decomposing the inner disk into a series of concentric circular rings of constant density (see Vorobyov & Basu 2006 for details). A more accurate method that is used in this paper involves an expansion of $\Phi_{\rm id}$ into Legendre polynomials in the plane of the disk. The details of this method will be given in a future paper. The total gravitational potential $\Phi = \Phi_{\rm disk}+\Phi_{\rm halo}+\Phi_{\rm id}$ is then used in the momentum equations.

3.2 Artificial viscosity

The artificial viscosity, much like kinematic viscosity in a real fluid, is often used to smooth discontinuities where the finite-difference equations break down. The 2nd order Boltzmann moment equations have to be modified to account for the viscous stresses and dissipation due to the artificial viscosity.

The implementation of the artificial viscosity in the kinetic model requires the use of a tensor formalism. The artificial viscosity stress tensor $\boldsymbol{Q}$ can be written by analogy to the general form of the molecular viscosity stress tensor

$$\boldsymbol{Q} = 2\mu_{\rm v}[\boldsymbol{\nabla u} - \frac{1}{3}(\boldsymbol{\nabla}\cdot\boldsymbol{u})\,\boldsymbol{e}], \quad (11)$$

where $\boldsymbol{\nabla u}$ is the symmetrized velocity gradient tensor, $\boldsymbol{\nabla}\cdot\boldsymbol{u}$ is the velocity divergence, $\boldsymbol{e}$ is the unit tensor, and $\mu_{\rm v}$ is coefficient of artificial viscosity defined as

$$\mu_{\rm v} = \begin{cases} L^2\Sigma\,\boldsymbol{\nabla}\cdot\boldsymbol{u} & \text{if } \boldsymbol{\nabla}\cdot\boldsymbol{u}<0 \\ 0 & \text{otherwise,}\end{cases}$$

where L is a constant with dimensions of length, chosen to be one zone width. The components of the artificial viscosity stress tensor $\boldsymbol{Q}$ in cylindrical coordinates are given in Appendix B. The off-diagonal components of $\boldsymbol{Q}$ are often set to zero to ensure that the artificial viscosity smoothes only compressible shock fronts and leaves large gradients of shear unchanged. The corresponding viscous stress and dissipation terms are introduced into the kinetic equations (4)-(8) by defining a generalized stress tensor $P_{ij} = \Sigma\sigma_{ij} + Q_{ij}$, where the artificial viscosity stress tensor Q_{ij} is analogous to the viscous stress tensor $-\pi_{ij}$ in gas dynamics. We note that Q_{ij} has a plus sign because the coefficient of artificial viscosity $\mu_{\rm v}$ is negative by definition. The modified momentum equations can be obtained from equations (4) and (5) by substituting $\Sigma\sigma_{rr}$ with P_{rr} and $\Sigma\sigma_{\phi\phi}$ with $P_{\phi\phi}$. The modified velocity dispersion equations can be derived by applying the same substitution to the last two terms of equations (6) and (7) and to the last three terms in equation (8).

3.3 Units

The units are chosen to be 10^{10} M$_\odot$ and 1 kpc for the mass and length scales, respectively. The gravitational constant G was set to 1. This results in a velocity unit of 207.4 km s^{-1} and a unit for the angular speed of 207.4 km s^{-1} kpc^{-1}. The time unit is 4.7 Myr. These units are used throughout the paper, unless other units are given explicitly.

3.4 Tests and accuracy

We performed several tests for our numerical code. Two standard tests – one focusing on the accuracy of the implementation of the advection and another one on the conservation of the specific angular momentum – are given in Appendix C in some detail. Both tests demonstrate the ability of the code to handle the advection terms numerically well, so that we do not expect spurious structure formation due to advection problems.

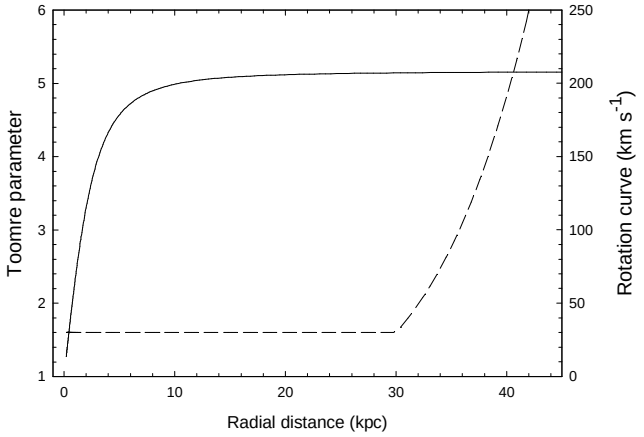

Figure 1. Initial profiles of the rotation curve (solid line, identical for all models), and Toomre parameter (dashed line, model K3) We note that the Q-profile just scales in different models.

Table 1. Model parameters of stellar disks

Model	Q_s	$\sigma_{rr}(r=0)$	$R_{\rm out}$ (kpc)
K1	1.1	112.5 km s^{-1}	30
K2	1.3	133 km s^{-1}	30
K3	1.6	164 km s^{-1}	45
K4	2.5	250 km s^{-1}	45
K5	3.15	315 km s^{-1}	45

3.5 Fourier amplitudes

In order to visualize the nature and growth of instabilities in disks, it is common to use the azimuthal Fourier modes $a_{\rm m}$ at a given radius r. They are calculated for $m \neq 0$ by (e.g. Laughlin et al. 1998)

$$a_{\rm m}(r,t) \equiv \frac{1}{2\pi} \left| \int_0^{2\pi} \Sigma(r,\phi,t) e^{im\phi} d\phi \right| . \quad (12)$$

An even simpler measure for the global structure of a disk are the (radially integrated) *global Fourier modes* defined by

$$C_{\rm m}(t) \equiv \frac{2\pi}{M_{\rm disk}} \int_{r_{\rm low}}^{r_{\rm high}} a_{\rm m}(r,t) r dr . \quad (13)$$

$M_{\rm disk}$ is the mass of the disk within the radial range $[r_{\rm low}, r_{\rm high}]$. The global Fourier amplitude A_m is the modulus of $C_{\rm m}$, whereas the global growth rate is given by the time derivative of the logarithmic Fourier amplitude, i.e.

$$\gamma_m \equiv \frac{d(\ln|C_{\rm m}(t)|)}{dt} . \quad (14)$$

4 RESULTS

4.1 Stability properties of non-isotropic (stellar) disks

The analysis of the stability of a *thin* stellar disk to a local *axisymmetric* perturbation states that the disk is stable if (Toomre 1964)

$$Q_{\rm s} \equiv \frac{\sigma_{rr}\kappa}{3.36 G\Sigma} > 1. \quad (15)$$

According to Polyachenko et al. (1997), the Toomre criterion (15) should be modified to $Q_{\rm s} > 2\pi\beta/3.36$, if local *non-axisymmetric* perturbations are considered. Here, β is a function of the rotation curve. In the most interesting case of a flat rotation curve, $\beta = 1.69$, so that a thin stellar disk becomes stable if $Q_{\rm s} \gtrsim 3.15$.

In this section we numerically study the stability properties of thin stellar disks characterized by different values of $Q_{\rm s}$. We do not focus on the detailed study of growth rates of unstable modes in the linear regime, since it would require a detailed comparison with previous analytical linear stability analyses. Instead, we simply compare the stability properties of stellar disks obtained using the BEADS-2D code with the analytical predictions of Polyachenko et al. (1997). By using the kinetic equations (3)-(8), we take full account of the inherent anisotropic properties of stellar disks. We present the results for five models, the parameters of which are shown in Table 1. The acronym K stand for "Kinetic models". The outer radii of stellar disks $R_{\rm out}$ were chosen so that to exclude the influence of the outer reflecting boundary. The surface density distribution and the rotation curve are identical for all models, while the initial velocity dispersion distributions are different. The surface density is distributed exponentially according to

$$\Sigma(r) = \Sigma_0 e^{-r/r_d}, \quad (16)$$

with a radial scale length r_d of 4 kpc. The central surface density Σ_0 is set to 10^3 M$_\odot$ pc^{-2}. Thus, the total mass of the disk within the 30 kpc radius is approximately 10^{11}M$_\odot$. We note that the densities of stellar disks are indeed found to decay exponentially with distance, with a characteristic scale length increasing from 2-3 kpc for the early type galaxies to 4-5 kpc in the late type galaxies (Freeman 1970). The initial azimuthal velocity is chosen according to equation (4), whereas the radial velocity vanishes initially. The radial component of the velocity dispersion is obtained from the relation $\sigma_{rr} = 3.36\, Q_{\rm s}\, G\, \Sigma/\kappa$ for a given value of the Toomre parameter $Q_{\rm s}$. We assume that throughout most of the disk $Q_{\rm s}$ is constant (and equal to the value given in Table 1) but is steeply increasing with radius at $r > 30$ kpc. The initial radial distribution of $Q_{\rm s}$ in model K3 is shown in Fig. 1 by the dashed line. The azimuthal component of the velocity dispersion $\sigma_{\phi\phi}$ is determined adopting the epicycle approximation, in which the following relation between $\sigma^2_{\phi\phi}$ and σ^2_{rr} holds (Binney & Tremaine 1987, p. 125):

$$\sigma^2_{\phi\phi} = \sigma^2_{rr} \cdot \frac{1}{2}\left(\frac{r}{u_\phi}\frac{du_\phi}{dr} + 1 \right). \quad (17)$$

The off-diagonal component $\sigma^2_{r\phi}$ is initially set to zero. In the beginning of simulations we introduce a small random perturbation with a maximum relative amplitude 10^{-5} to the initial density distribution.

Figure 2 shows the temporal behaviour of the dominant $m = 2$ mode in models K1-K5 with different initial values of the Q-parameter. It is evident that models with initially larger $Q_{\rm s}$ attain the saturation phase at later times than do the models with smaller $Q_{\rm s}$. For instance, in model K2 ($Q_{\rm s} = 1.3$) the saturation of the dominant mode is reached after 1.4 Gyr, whereas in model K1 ($Q_{\rm s} = 1.1$) the dominant mode saturates at an earlier time $t = 0.8$ Gyr. Model K4 with the initial $Q_{\rm s} = 2.5$ reaches the saturation phase only after approximately 7 Gyr. The global Fourier amplitudes in

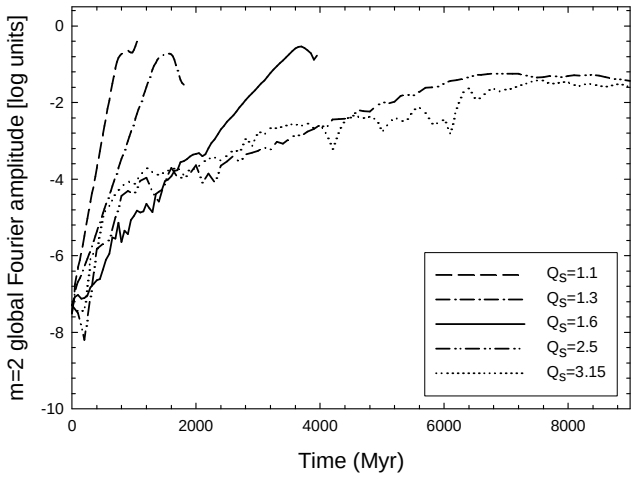

Figure 2. The temporal behaviour of the $m = 2$ mode in kinetic models with different initial Q-parameters: $Q_{\rm s} = 1.1$ (K1), 1.3 (K2), 1.6 (K3), 2.5 (K4), and 3.15 (K5).

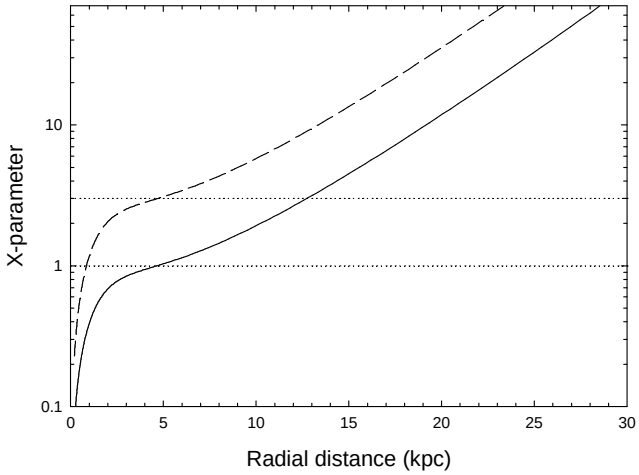

Figure 3. The initial radial distributions of the X-parameter for the $m = 1$ mode (dashed line) and the $m = 2$ mode (solid line). Note that X is identical in all five models listed in Table 1, because these models initially differ only in the values of the velocity dispersion.

the saturation phase are noticeably larger in models K1–K3 ($C_2(t) \approx 0.1 - 0.25$) than in models K4 and K5 ($C_2(t) \approx 0.02 - 0.05$), indicating a stronger instability in colder disks.

The linear stability analysis of non-isotropic stellar disks to local perturbations performed by Polyachenko et al. (1997) yields a critical value of $Q_{\rm s,crit} \approx 3.15$ for stellar disks with a flat rotation curve. Our numerical simulations indicate that the $m = 2$ mode in the $Q_{\rm s} = 3.15$ model K5 saturates at a very low level of $C_2 \approx 0.02 - 0.03$. As we shall see in § 4.3, stellar disks characterized by such small values of C_2 can only develop a clumpy pattern with very small positive density perturbations rather than a spiral pattern or a bar.

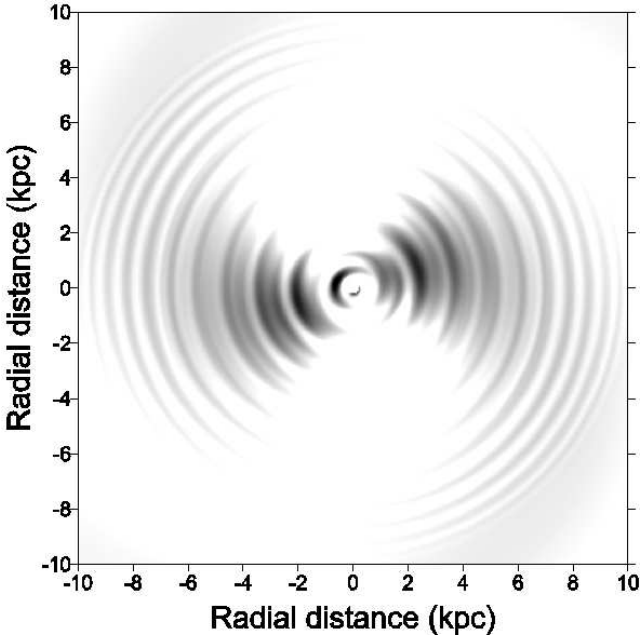

Figure 4. The positive density perturbation that develops in the inner 10 kpc region in model K2 at $t = 1.0$ Gyr. The lumpy structure is naturally explained as the result of interference between leading and trailing short-wavelength disturbances that propagate through the centre of the disk. The scale bar is in $M_\odot$ pc^{-2}.

4.2 Swing amplification

An appealing physical interpretation for the growth of strong instabilities that are common in numerical simulations of differentially rotating stellar disks is swing amplification (Toomre 1981). Amplification occurs when any leading disturbance unwinds into a trailing one due to differential rotation. It is helpful to introduce the parameter $X \equiv \lambda/\lambda_{\rm cr}$ when discussing the efficiency of swing amplification, where $\lambda \equiv 2\pi r/m$ is the circumferential wavelength of an m-armed disturbance and $\lambda_{\rm cr} \equiv 4\pi^2 G\Sigma/\kappa^2$ is the longest unstable wavelength in a cold disk. According to Julian and Toomre (1966), in a stellar disk with a flat rotation curve the gain of the swing amplifier is the largest when $1 < X < 3$. The gain also strongly depends on the value of the Q-parameter. Substantial amplification is also possible for $X < 1$ if Q is safely below 2.

Figure 3 shows the initial radial distribution of the X-parameter for the $m = 1$ (dashed line) and $m = 2$ (solid line) disturbances. It is evident that the best conditions for swing amplification ($1 < X < 3$) of the $m = 1$ mode are met in the inner portion of the disk at $(0.85 - 4.7)$ kpc, while the swing amplifier of the $m = 2$ mode is maximal at intermediate radii $(4.7 - 12.8)$ kpc. However, feedback loops that turn leading disturbances into trailing ones must be present in stellar disks in order for swing amplification to destabilize the disk (see e.g. BT87 for a discussion). Since our stellar disks (initially) have no inner Lindblad resonances, the trailing disturbances can propagate through the centre and emerge on the other side as leading ones, thus providing a feedback for the swing amplifier. Figure 4 supports this point of view. It shows the positive density perturbation that develops in the inner 10 kpc in model K2 after 1 Gyr from the beginning of simulations. The lumpy structure that is seen

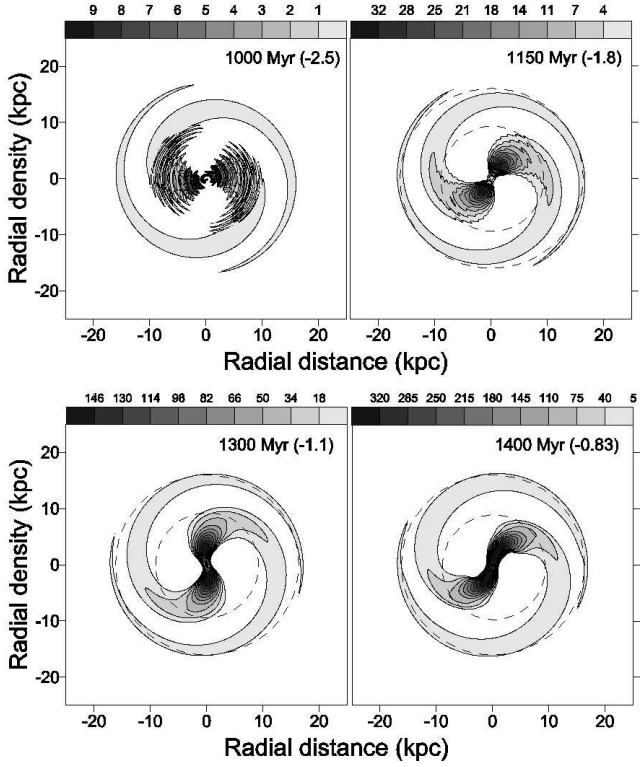

Figure 5. Positive density perturbations in model K2 at four different times indicated in each panel. The quantities in parentheses give the values of $C_2(t)$ (in log units) at the corresponding evolutionary times. The outer and inner dashed circles sketch the positions of corotation and the outer Lindblad resonances. The scale bars give the positive density perturbations in $M_\odot$ pc^{-2}.

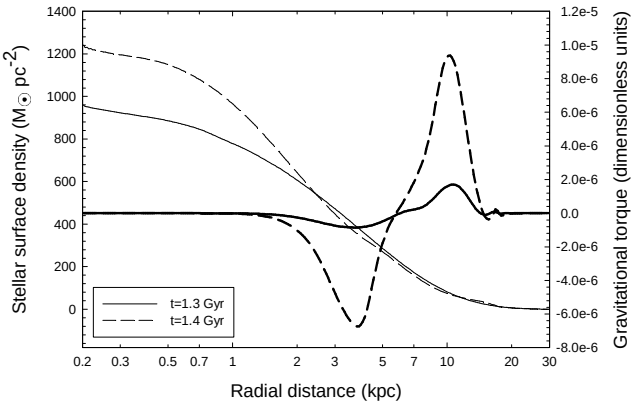

Figure 6. The azimuthally averaged surface density distribution of stars (thin solid and dashed lines) and the azimuthally averaged gravitational torque (thick solid and dashed lines) obtained in model K2 at two different evolutionary times as indicated in the legend.

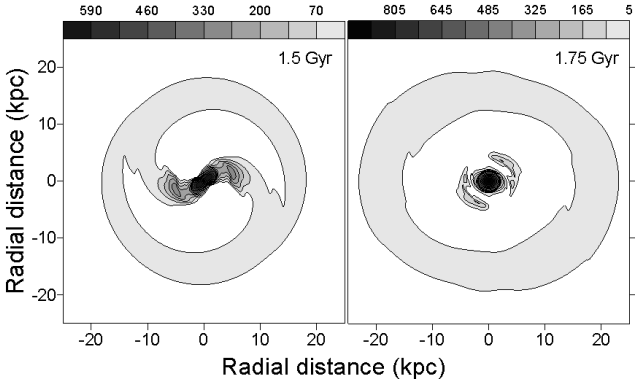

Figure 7. Positive density perturbations in model K2 at 1.5 Gyr (left panel) and 1.75 Gyr (right panel). The scale bar is in $M_\odot$ pc^{-2}.

in Fig. 4 is naturally explained as the result of interference between leading and trailing short-wavelength ($\lambda < \lambda_{\rm cr}$) disturbances, propagating through the disk centre. A similar phenomenon was seen in the numerical modelling by Toomre (1981) and was discussed by BT87 (cf. Sect. 6.3, 2(c)). The $m = 1$ density response dominates the innermost disk, while the $m = 2$ density perturbation is the strongest in the intermediate and outer regions in Fig. 4. This tendency can indeed be expected from the radial distribution of the X-parameter for the $m = 1$ and $m = 2$ modes shown in Fig. 3. The perturbation amplitudes gradually decline at larger radii.

To better illustrate the development of the $m = 2$ instability, we plot in Fig. 5 the positive density perturbation obtained in model K2 at four different times. The quantities in parentheses give the global Fourier amplitudes (in log units) at the corresponding times, while the scale bars give the amplitudes of positive density perturbations in $M_\odot$ pc^{-2}. It is clearly seen that the $m = 2$ mode is the fastest growing mode. The lumpy structure at $t = 1$ Gyr is gradually transforming into an $m = 2$ spiral perturbation at $t = 1.15$ Gyr. The spiral perturbation is mostly localized within the outer Lindblad resonance (OLR; shown by the outer dashed circle), which is in good agreement with the theoretical predictions.

As the global Fourier amplitude $C_2(t)$ exceeds 0.1 at $t \approx 1.3$ Gyr, the subsequent evolution of the $m = 2$ spiral disturbance is governed by the non-linear effects of mass and angular momentum redistribution in the disk. Spiral disturbances are known to transfer mass inward and angular moment outward (see e.g. Laughlin et al. 1997). The azimuthally averaged gravitational torque $\Gamma(r)$, which is the sum of the individual torques $\tau = -m\,\partial\Phi/\partial\phi$ exerted on all computational cells at a given radius r, is known to be a good diagnostic tool for the mass and angular momentum redistribution in the disk. Figure 6 shows $\Gamma(r)$ and the azimuthally averaged surface density distribution in model K2 obtained at $t = 1.3$ Gyr and $t = 1.4$ Gyr. The stars that are characterized by negative Γ are losing angular momentum and spiralling into the centre, while the stars that are distinguished by positive Γ are gaining angular momentum and moving radially outward. As a result, the density in the central region starts to grow considerably after 1.3 Gyr, which triggers the formation of a transient bar inside corotation. This process is evident in the right lower panel of Fig. 5. The material that flows radially outward settles into a weak outer resonant ring near the position of the outer Lindblad resonance at approximately 15 kpc (note that Γ becomes zero outside the outer Lindblad resonance).

A shortage of matter that develops in the intermediate region weakens the spiral structure and terminates the mass

Table 2. Pattern speeds and position of resonances

Model	$\Omega_{\rm p}^{(a)}$	CR	OLR
K1	30.2	6.2	11.5
K2	23.1	8.4	15
K3	19.1	10.4	18.1
K4	11.5	17.6	24.1

$^{(a)}$ the pattern speeds are in km s^{-1} kpc^{-1} and positions of corotations (CR) and outer Lindblad resonances (OLR) are in kpc.

and angular momentum redistribution. In the end, the bar transforms into a compact dense central disk, while the spiral structure virtually disappears. The outer resonant ring occupies a substantial portion of the outer disk. Figure 7 illustrates this process and shows the positive density perturbation that develops in model K2 at $t = 1.5$ Gyr (left) and $t = 1.75$ Gyr (right). This phenomenon is a nice example of the dominant mode self-interaction originally studied by Laughlin et al. (1997) in the context of gaseous disks.

4.3 Stabilization at larger $Q_{\rm s}$

The stabilizing effect of increasing $Q_{\rm s}$ is clearly seen in Fig. 2. The $m = 2$ perturbations in hotter disks are characterized by lower growth rates and they take longer time to saturate. The global Fourier amplitudes in the saturation phase are noticeably larger in models K1–K3 ($C_2(t) \approx 0.1 - 0.25$) than in models K4 and K5 ($C_2(t) \approx 0.02 - 0.05$), indicating a weaker instability for hotter disks. Figure 8 shows the positive density perturbation that develops in model K4 in the saturation phase at 6.8 Gyr (left panel) and 7.0 Gyr (right panel). The bar and the spiral arms have a patchy, flocculent appearance. The positive density perturbation (in physical units of $M_\odot$ pc^{-2}) in the saturation phase is on average *an order of magnitude smaller* than in model K2 (Fig. 5). Clearly, the growth of the global modes is considerably suppressed in model K4. Figure 9 shows the positive density perturbation that develops in model K5 in the saturation phase at 7.6 Gyr (left panel) and 8.8 Gyr (right panel). It is obvious that the positive density perturbation in model K5 is characterized by a clumpy structure of low amplitude rather than by a regular spiral or bar. This is because in model K5 both the $m = 1$ and $m = 2$ modes saturate at a nearly equal (and very small) value of $C_{1,2} \approx 0.02 - 0.03$. Thus, we confirm the theoretical predictions of Polyachenko et al. (1997), who have analytically shown that stellar disks characterized by $Q_{\rm s} < 3.15$ and a flat rotation curve are unstable to local density perturbations.

We have shown in Sect. 4.2 that the physical interpretation for the instability growth in our models is swing amplification, with the feedback provided by the trailing disturbances propagating through the disk centre. Julian and Toomre (1966) have shown that the gain of swing amplification is greatly sensitive to the values of the X- and Q-parameters. More specifically, the gain diminishes considerably for $Q_{\rm s} > 2$. Since the initial radial profiles of the X-parameter are identical in all model disks (see Fig. 3), the increase in $Q_{\rm s}$ and, by implication, in random motions

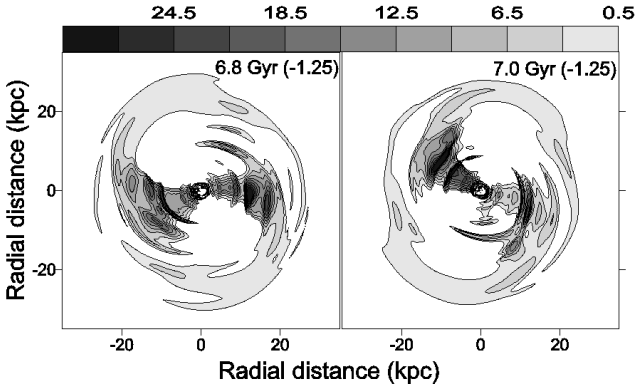

Figure 8. Positive density perturbations in model K4 at 6.8 Gyr (left panel) and 7.0 Gyr (right panel). The quantities in parentheses give the values of $C_2(t)$ (in log units) at the corresponding evolutionary times. Note a patchy, flocculent structure of the bar and spiral arms. The scale bar is in $M_\odot$ pc^{-2}.

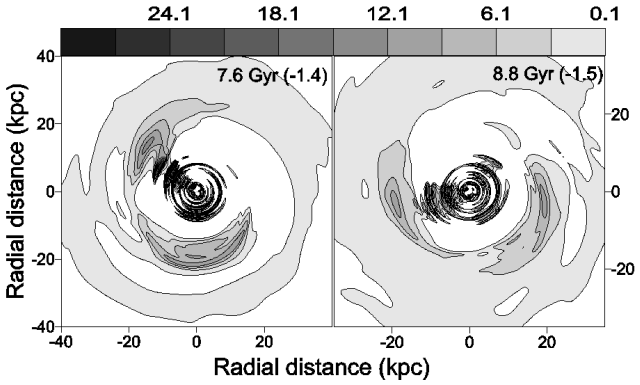

Figure 9. The same as in Fig. 8 but for model K5.

of stars suppresses the short-wavelength disturbances and thus inhibits the swing amplifier.

The comparison of dynamical properties of our model disks suggests another stabilization effect that may be present in hotter stellar disks. Table 2 gives the pattern speeds and the positions of corotation and outer Lindblad resonances in models K1–K4. These values are computed in the saturation phase and may slightly change during the evolution. It is clearly seen that models with larger $Q_{\rm s}$ are distinguished by a slower pattern speed $\Omega_{\rm p}$. This is in qualitative agreement with the predictions of the linear stability analysis of round galactic disks by Pichon & Cannon (1997), who have shown that colder disks yield more centrally concentrated and faster rotating spirals. Slower pattern speeds in hotter disks imply that the latter can easier develop the inner Lindblad resonance due to the rearrangement of mass and angular momentum. Indeed, solid lines in Fig. 10 show the initial radial profiles of stellar angular velocity Ω and quantities $\Omega \pm \kappa/2$, while the dashed lines give the pattern speeds $\Omega_{\rm p}$ in models K1–K4 (from top to bottom). None of the models have the inner Lindblad resonance but the tendency is clear: hotter disks have better chances for the inner Lindblad resonance to occur. The inner Lindblad resonance would prohibit the propagation of spiral disturbances through the disk centre, thus providing the cutoff for the swing amplification feedback.

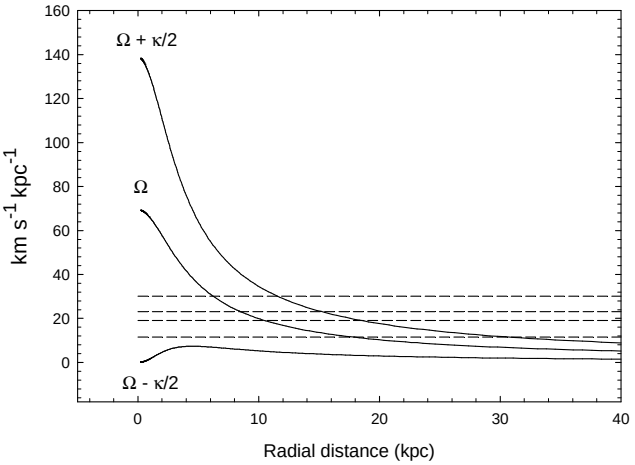

Figure 10. Radial profiles of the stellar angular velocity Ω (dotted-dashed line) and quantities $\Omega \pm k/2$. The pattern speeds $\Omega_{\rm p}$ of models K1–K4 are shown by the dashed lines (from top to bottom).

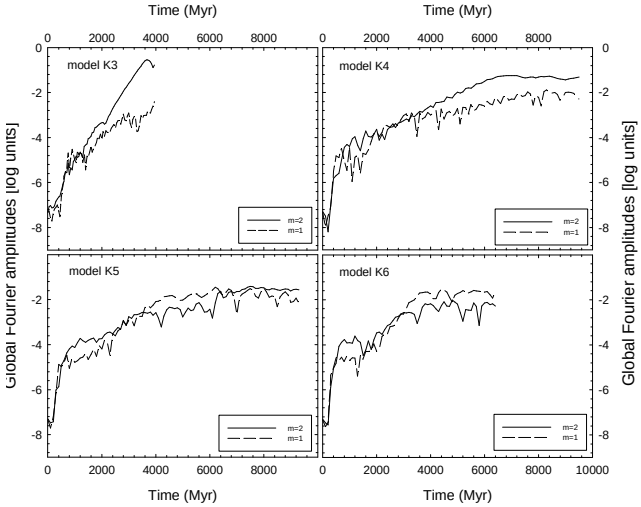

Figure 11. Temporal evolution of the $m = 1$ modes (dashed lines) and the $m = 2$ modes (solid lines) in models K3, K4, K5, and K6. Model K6 is characterized by $Q_{\rm s} = 3.5$. Note that in the saturation phase the global Fourier amplitudes of the $m = 2$ modes decrease along the sequence of increasing $Q_{\rm s}$, while the global Fourier amplitudes of the $m = 1$ modes stay nearly constant in all four models.

4.4 The $m = 1$ density perturbation

The initial radial distributions of the X-parameter in Fig. 3 (identical for all our model disks) suggest that the $m = 1$ perturbations should dominate in the innermost parts of stellar disks. In fact, this can already be seen in Fig. 4, where the positive density response in the inner 1 kpc has a crescent shape. We find that hotter disks are more strongly disposed to the development of the $m = 1$ density perturbations than colder disks. Although the instability in disks with $Q_{\rm s} \lesssim 2.5$ is dominated by the symmetric $m = 2$ mode, the lopsided $m = 1$ mode in disks with $Q_{\rm s} > 2.5$ may compete with or even prevail over the $m = 2$ mode. This tendency is clearly seen in Fig. 11, in which we show the temporal evolution of the $m = 1$ mode (dashed lines) and $m = 2$ mode (solid lines) in models K3–K6. Model K6 is initially characterized by $Q_{\rm s} = 3.5$. It is obvious that the $m = 2$ mode dominates during the evolution (except for the very early phase) in models with $Q_{\rm s} = 1.6$ (K3) and $Q_{\rm s} = 2.5$ (K4). This tendency is not seen in the $Q_{\rm s} = 3.15$ model K5, in which both the $m = 1$ and $m = 2$ modes have a nearly equal global Fourier amplitudes and growth rates in the saturation phase. Finally, the $Q_{\rm s} = 3.5$ model K6 is characterized by the dominant $m = 1$ mode.

The preponderance of the $m = 1$ mode in model K6 is due to the fact that one-armed perturbations are much more difficult to stabilize (Evans & Read 1998). Indeed, the $m = 1$ modes have no inner Lindblad resonance (the quantity $\Omega - \kappa$ is negative), which removes a powerful stabilizing effect for the $m = 1$ mode. On the other hand, the stabilizing effect of the inner Lindblad resonance for the $m = 2$ mode is expected to become stronger along the sequence of increasing $Q_{\rm s}$ (see Fig. 10). As a consequence, the strength of the $m = 2$ mode in the saturation phase (as determined by $C_2(t)$) decreases for hotter disks, whereas the strength of the $m = 1$ mode (as determined by $C_1(t)$) stays nearly constant in all four models shown in Fig. 11. We note that according to Evans & Read (1998) stellar disks with a sharp central cut-out (stellar density drops to zero in the centre) are much more unstable to the development of the $m = 1$ modes.

4.5 Vertex deviation

The non-isotropic nature of the BEADS-2D code allows for a numerical study of the velocity ellipsoid properties in spiral galaxies. The non-axisymmetric component of the spiral gravitational field may produce considerable perturbations on stellar orbits. A vertex deviation $l_{\rm v}$ can be used to study the magnitude of the spiral gravitational field (Kuijken & Tremaine 1994). The vertex deviation has a simple geometric interpretation: it is the angle between the major axis of the velocity ellipsoid (the surface that has semi-axes σ_{zz}, σ_{rr}, and $\sigma_{\phi\phi}$) at a given position in the disk and the centre-anticentre direction. Based on the above explanation, the value of $l_{\rm v}$ can be defined as (Binney and Merrifield 1998, p. 630)

$$l_{\rm v} = \frac{1}{2}\mathrm{atan}\left(\frac{2\sigma_{r\phi}^2}{\sigma_{rr}^2 - \sigma_{\phi\phi}^2}\right). \qquad (18)$$

This definition is incomplete because it implicitly assumes the epicycle approximation, i.e $\sigma_{rr}^2 > \sigma_{\phi\phi}^2$. As a result, the value of $l_{\rm v}$ is limited to the $[-45^\circ, 45^\circ]$ range depending on the sign of $\sigma_{r\phi}^2$. As a matter of fact, the epicycle approximation may break down in the presence of a strong non-axisymmetric gravitational field of spiral arms. Consequently, the azimuthal dispersion may become (locally) larger than the radial one and the angle between the major axis of the velocity ellipsoid and the centre-anticentre direction may exceed $\pm 45^\circ$. To take this possibility into account, we extend the definition of the classical vertex deviation as follows:

$$\tilde{l}_{\rm v} = \begin{cases} l_{\rm v} & \text{if } \sigma_{rr}^2 > \sigma_{\phi\phi}^2 \\ l_{\rm v} + \mathrm{sign}\left(\sigma_{r\phi}^2\right) \cdot \dfrac{\pi}{2} & \text{if } \sigma_{rr}^2 < \sigma_{\phi\phi}^2. \end{cases}$$

Black dashes in Fig. 12 show the major axes of the velocity ellipsoids superimposed on the positive density perturbation map which is obtained in model K2 at $t = 1.4$ Gyr. Con-

siderable vertex deviations are seen near the convex edges of spiral perturbations and near the bar, where $\tilde{l}_{\rm v}$ may become as high as 89°. Interestingly, the concave edges of spiral perturbations do not produce noticeable vertex deviations. The outer axisymmetric regions and the inter-arm regions are also characterized by near-zero vertex deviations. The temporal evolution of a mass-weighted value of $\tilde{l}_{\rm v}$ over the entire disk is approximately correlated with $C_2(t)$. For instance $l_{\rm v} = 1.8^\circ$ at $t = 1.0$ Gyr and $l_{\rm v} = 12.6^\circ$ at $t = 1.4$ Gyr.

Since we start our simulations with a zero vertex deviation ($\sigma_{r\phi} = 0$), we confirm that the spiral gravitational field produces a vertex deviation – a conclusion previously made by Kuijken & Tremaine (1994) on analytical grounds. A more detailed study of the properties of the velocity ellipsoids in spiral galaxies will be presented in a forthcoming paper.

In contrast to gaseous disks, stellar disks are essentially non-isotropic. In the epicycle approximation, the ratio of radial to azimuthal components of the velocity ellipsoid can be described by equation (17), implying that stellar disks are colder in the azimuthal direction than in the radial direction. The initial ratios $\sigma_{\phi\phi} : \sigma_{rr}$ in model K2 lie in the $(1 - 0.71)$ range, with the minimum and maximum values being near the centre and at the outer edge of the stellar disk, respectively. As the disk evolves and the spiral structure emerges, the ratios $\sigma_{\phi\phi} : \sigma_{rr}$ start to show considerable deviations from the initial values. In the saturation phase, the bulk of the stellar disk is characterized by $\sigma_{\phi\phi} : \sigma_{rr}$ lying in the $0.65 - 0.75$ range, which is comparable to a measured mean value of $\sigma_{\phi\phi} : \sigma_{rr} \approx 0.8$ for the disk of NGC 488 (Gerssen et al. 1997). However, considerably smaller values of $\sigma_{\phi\phi} : \sigma_{rr} \lesssim 0.4$ are found at the leading edges of spiral arms, implying that the epicycle approximation breaks down there. A more detailed study of the anisotropy of the velocity ellipsoid will be presented in a future paper.

4.6 Miscellaneous

In all models considered in this paper, the outer reflecting boundary is set at a large enough distance ($r \gtrsim 30$ kpc) so as to exclude its influence on spiral generation and growth. A factor of 2 variation in the position of the inner reflecting boundary (0.2 kpc in the present simulation) does not introduce a noticeable change in the numerical results. The radial and azimuthal components of velocity dispersions may accidentally become negative in the late saturation phase, probably due to large gradients of the stellar potential. In that case the time step is reduced and the solution is sought again. In the rare case that this procedure fails to resolve the problem, we set the velocity dispersion in particular computational cells to a predefined small value.

Our simulations have shown that artificial viscosity is usually not needed in models with $Q_{\rm s} \gtrsim 1.3$. However, the artificial viscosity has to be included if the evolution of spiral instabilities is followed deeply into the nonlinear regime in models with $Q_{\rm s} < 1.3$. The solution is only slightly modified by the artificial viscosity. For instance, the relative difference in the growth rate of the dominant $m = 2$ mode in model K1 with and without artificial viscosity is kept below 2% during the simulations.

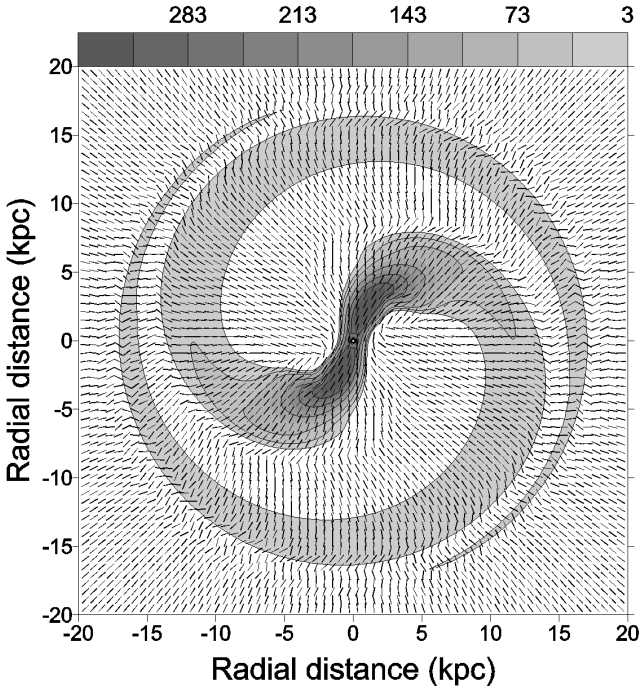

Figure 12. The major axes of velocity ellipsoids superimposed on the surface density distribution of the kinetic model K2 ($Q_s = 1.3$) at the time $t = 1.3$ Gyr. The angle between the major axis of velocity ellipsoid and the centre-anticentre direction ($\phi = const$) gives a value of vertex deviation.

5 SUMMARY AND CONCLUSIONS

We have developed the Boltzmann moment equation approach for the dynamics of stars (BEADS-2D), which is a finite-difference Eulerian code based on the Boltzmann moment equations up to second order. We adopt the zero-heat-flux approximation to close the system of moment equations. The BEADS-2D code is formulated in the polar coordinates (r, ϕ), which makes it most suitable for the numerical modelling of flattened galactic stellar disks. By calculating the tensor of the velocity dispersions, we can follow the anisotropy and the vertex deviation of the stellar system. Compared to numerical codes assuming a polytropic equation of state (see e. g. Korchagin et al. 2000), the BEADS-2D code allows for a larger variety of simulations, because the mass and velocity dispersion profiles can be chosen independently. For the reader's convenience, we provide the full set of three-dimensional Boltzmann moment equations up to second order in Appendix A . These equations are formulated in the cylindrical coordinates (z, r, ϕ) using the usual zero-heat-flux approximation and are suitable for a global modelling of galactic disks without simplifying geometry assumptions.

As an example of the utility of the BEADS-2D code, we study the time-dependent evolution of exponential stellar disks characterized initially by different values of the Toomre parameter $Q_{\rm s}$. The disks are embedded in a static dark matter halo, yielding a nearly flat rotation curve (except for the innermost several kiloparsecs characterized by rigid rotation). Specifically, we find the following.

(i) We confirm the results of linear stability analysis by Polyachenko et al. (1997), who obtained a stability thresh-

old value of $Q_s \approx 3.15$ for stellar disks with a *purely* flat rotation curve. A physical interpretation for the instability is swing amplification of short-wavelength trailing disturbances, which propagate through the disk centre and provide a feedback mechanism for the swing amplifier.

(ii) The character of the instability is distinct in the linear and nonlinear regimes, the tentative boundary between which we define by the global Fourier amplitude $C_2(t) = 0.1$. As a reference model, we investigated a stellar disk with $Q_s = 1.3$. In the early linear phase, instability demonstrates a typical lumpy pattern, which grows in amplitude with time and gradually transformes in to a global two-armed spiral in the late linear phase. This lumpy pattern results most probably from the interference between leading and trailing disturbances, propagating through the disk centre. A similar phenomenon is discussed in Binney & Tremaine (1987) in connection with the numerical simulations of Toomre (1981). In the nonlinear phase, the redistribution of mass and angular momentum by the gravitational torques of spiral arms comes into play. The gravitational torques produce an inflow of mass, which forms a transient central bar inside corotation, and an outflow of mass, which forms a ring at the OLR. This process of mass redistribution continues until the two-armed spiral is weakened by the shortage of matter. Finally, a transient bar is transformed into the compact dense central disk and the spiral arms virtually disappear, leaving only the outer diffuse ring at the OLR.

(iii) The instability in disks with $Q_s \lesssim 2.5$ is mostly dominated by the symmetric $m = 2$ mode, while the lopsided $m = 1$ mode in disks with $Q_s > 2.5$ may compete with or even prevail over the $m = 2$ mode. This is due the fact that the $m = 1$ mode has no inner Lindblad resonance, which makes it difficult to stabilize. On the other hand, the stabilizing effect of the inner Lindblad resonance on the $m = 2$ mode is expected to grow along the sequence of increasing Q_s.

(iv) Stellar disks near a stability limit of $Q_s = 3.15$ still develop a clumpy structure. However, both the growth timescales (comparable to the Hubble time) and the small amplitudes of positive density perturbations make such instabilities difficult to observe at best.

(v) Stellar disks are stabilized by one or more of the following procedures. a) An increase in the stellar velocity dispersions suppresses the growth of short-wavelength density perturbations and thus inhibits the swing amplifier. b) Slower pattern speeds in hotter disk make it more likely for the inner Lindblad resonance to occur, thus providing the cutoff for the sing amplification feedback.

The presence of the non-diagonal velocity dispersion terms in the Boltzmann moment equations allows us to study the vertex deviation. In most regions of the stellar disk the velocity ellipsoid is well aligned with the radial axes of the polar grid. In agreement with analytical predictions by Kuijken & Tremaine (1994), considerable vertex deviations show up in regions with strongly perturbed mass distributions, i.e. near the spiral arms. The vertex deviations are large at the convex edge of the spiral arms, whereas they are small at the concave edge. The mean vertex deviations correlate well with the global Fourier amplitudes. Near the convex edge of the spiral arms, the ratio of radial to azimuthal components of the velocity ellipsoid can deviate considerably from the values predicted from the epicycle approximation. A more detailed numerical study of the properties of velocity ellipsoids in spiral galaxies will be presented in a future paper.

ACKNOWLEDGMENTS

We would like to thank the referee for several important suggestions, especially for pointing out the motivation of this paper more clearly. The authors are grateful to Prof. Shantanu Basu for carefully reading the manuscript, correcting the English language usage, and suggesting stylistical improvements. A research visit of EIV has been supported by a grant of the University of Vienna. EIV also gratefully acknowledges present support from a CITA National Fellowship. Our special thanks are to Prof. Martin Houde for generously providing computational facilities.

REFERENCES

Amendt, P., Cuddeford, P., 1991, ApJ, 368, 79
Aoki, S., Noguchi, M., Iye, M., 1979, PASJ, 31, 737
Basu, S., 1997, ApJ, 485, 240
Bertin, G., Lin, C.C., Lowe S.A., Thurstans, R.P., 1989, ApJ, 338, 104
Binney, J., Tremaine, S., 1987, Galactic Dynamics, Princeton Univ. Press
Binney, J., Merrifield, M. S., 1998, Galactic Astronomy, Princeton Univ. Press
Cuddeford, P., Amendt, P., 1991, MNRAS, 253, 427
Evans, N. W., Read, J. C. A., 1998, MNRAS, 300, 106
Freeman, K. C., 1970, ApJ, 160, 811
Gerssen J., Kuijken K., Merrifield M. P., 1997, MNRAS, 288, 618
Giersz, M., Spurzem, R., 1994, MNRAS, 269, 241
Julian, W. H., Toomre, A., 1966, ApJ, 146, 810
Kuijken, K., Tremaine, S., 1994 ApJ, 421, 178
Korchagin, V.I., Kikuchi, N., Miyama, S.M., et al., 2000, ApJ, 541, 565
Jalali, M. A., Hunter, C., 2005, ApJ, 630, 804
Larson, R.B., 1970, MNRAS, 147, 323
Laughlin, G., Korchagin, V., Adams, F.C., 1997, ApJ, 477, 410
Laughlin, G., Korchagin, V., Adams, F.C., 1998, ApJ, 504, 945
Louis, P., 1990, MNRAS, 244, 478
Norman, M. L., Wilson, J. R., Barton, R. T., 1980, ApJ, 239, 968
Orlova, N., Korchagin, V.I., Theis, Ch., 2002, A&A, 384, 872
Pichon, C., Cannon, R. C., 1997, MNRAS, 291, 616
Polyachenko, V. L., Polyachenko, E. V., Strel'nikov, A. V., 1997, Astron. Zhurnal, 23, 598 (translated Astron. Lett. 23, 525)
Samland, M., Hensler, G., Theis, Ch., 1997, ApJ, 476, 544
Stone, J. M., Norman, M. L., 1992, ApJS, 80, 753
Theis, Ch., Burkert, A., Hensler, G., 1992, A&A, 265, 465
Toomre, A., 1964, ApJ, 139, 1217
Toomre, A., in Fall S. M., Lynden-Bell D., eds., The Structure and Evolution of Normal Galaxies. Cambridge Univ. Press, Cambridge

Vorobyov, E. I., Basu, S., 2006, ApJ, in press
Zang, t. A., 1976, PhD thesis, Massachusetts Institute of Technology

APPENDIX A: THE 3D-BOLTZMANN MOMENT EQUATIONS UP TO SECOND ORDER

The Boltzmann moment equations (up to second order) read in cylindrical coordinates (r, ϕ, z) as:

Continuity equation:

$$\frac{\partial \rho}{\partial t} + \frac{1}{r}\frac{\partial}{\partial r}(r \cdot \rho \cdot u_r) + \frac{1}{r}\frac{\partial}{\partial \phi}(\rho \cdot u_\phi) + \frac{\partial}{\partial z}(\rho \cdot u_z) = 0. \quad \text{(A1)}$$

Momentum equations:

$$\begin{aligned}\frac{\partial}{\partial t}(\rho u_z) &+ \frac{1}{r}\frac{\partial}{\partial r}(r \cdot \rho u_z \cdot u_r) + \frac{\partial}{\partial z}(\rho u_z \cdot u_z) \\ &+ \frac{1}{r}\frac{\partial}{\partial \phi}(\rho u_z \cdot u_\phi) + \frac{\partial}{\partial z}(\rho \sigma_{zz}^2) \\ &+ \frac{1}{r}\frac{\partial}{\partial r}(r \cdot \rho \sigma_{zr}^2) + \frac{1}{r}\frac{\partial}{\partial \phi}(\rho \sigma_{z\phi}^2) + \rho\frac{\partial \Phi}{\partial z} = 0, \quad \text{(A2)}\end{aligned}$$

$$\begin{aligned}\frac{\partial}{\partial t}(\rho u_r) &+ \frac{\partial}{\partial z}(\rho u_r \cdot u_z) + \frac{1}{r}\frac{\partial}{\partial r}(r \cdot \rho u_r \cdot u_r) \\ &+ \frac{1}{r}\frac{\partial}{\partial \phi}(\rho u_r \cdot u_\phi) - \frac{\rho u_\phi^2}{r} + \frac{\partial}{\partial z}(\rho \sigma_{rz}^2) \\ &+ \frac{1}{r}\frac{\partial}{\partial r}(r \cdot \rho \sigma_{rr}^2) + \frac{1}{r}\frac{\partial}{\partial \phi}(\rho \sigma_{r\phi}^2) - \frac{\rho \sigma_{\phi\phi}^2}{r} \\ &+ \rho\frac{\partial \Phi}{\partial r} = 0, \quad \text{(A3)}\end{aligned}$$

$$\begin{aligned}\frac{1}{r}\Big[\frac{\partial}{\partial t}(\rho r u_\phi) &+ \frac{1}{r}\frac{\partial}{\partial r}(r \cdot \rho r u_\phi \cdot u_r) + \frac{1}{r}\frac{\partial}{\partial \phi}(\rho r u_\phi \cdot u_\phi) \\ &+ \frac{\partial}{\partial z}(\rho r u_\phi \cdot u_z)\Big] + \frac{\partial}{\partial z}(\rho \sigma_{\phi z}^2) \\ &+ \frac{\partial}{\partial r}(\rho \sigma_{r\phi}^2) + \frac{1}{r}\frac{\partial}{\partial \phi}(\rho \sigma_{\phi\phi}^2) + \frac{2}{r}\rho \sigma_{r\phi}^2 \\ &+ \rho\frac{1}{r}\frac{\partial \Phi}{\partial \phi} = 0. \quad \text{(A4)}\end{aligned}$$

Velocity dispersion equations:

$$\begin{aligned}\frac{\partial}{\partial t}(\rho \sigma_{zz}^2) &+ \frac{1}{r}\frac{\partial}{\partial r}(r \cdot \rho \sigma_{zz}^2 \cdot u_r) + \frac{\partial}{\partial z}(\rho \sigma_{zz}^2 \cdot u_z) \\ &+ \frac{1}{r}\frac{\partial}{\partial \phi}(\rho \sigma_{zz}^2 \cdot u_\phi) + 2\rho \sigma_{rz}^2\frac{\partial u_z}{\partial r} + 2\rho \sigma_{zz}^2\frac{\partial u_z}{\partial z} \\ &+ 2\rho \sigma_{z\phi}^2\frac{1}{r}\frac{\partial u_z}{\partial \phi} = 0, \quad \text{(A5)}\end{aligned}$$

$$\begin{aligned}\frac{\partial}{\partial t}(\rho \sigma_{rr}^2) &+ \frac{1}{r}\frac{\partial}{\partial r}(r \cdot \rho \sigma_{rr}^2 \cdot u_r) + \frac{\partial}{\partial z}(\rho \sigma_{rr}^2 \cdot u_z) \\ &+ \frac{1}{r}\frac{\partial}{\partial \phi}(\rho \sigma_{rr}^2 \cdot u_\phi) + 2\rho \sigma_{rr}^2\frac{\partial u_r}{\partial r} + 2\rho \sigma_{rz}^2\frac{\partial u_r}{\partial z} \\ &+ 2\rho \sigma_{r\phi}^2\frac{1}{r}\frac{\partial u_r}{\partial \phi} - \frac{4\rho \sigma_{r\phi}^2 u_\phi}{r} = 0, \quad \text{(A6)}\end{aligned}$$

$$\begin{aligned}\frac{\partial}{\partial t}(\rho \sigma_{\phi\phi}^2) &+ \frac{1}{r}\frac{\partial}{\partial r}(r \cdot \rho \sigma_{\phi\phi}^2 \cdot u_r) + \frac{\partial}{\partial z}(\rho \sigma_{\phi\phi}^2 \cdot u_z) \\ &+ \frac{1}{r}\frac{\partial}{\partial \phi}(\rho \sigma_{\phi\phi}^2 \cdot u_\phi) + \frac{2\rho \sigma_{\phi\phi}^2 u_r}{r} + \frac{2\rho u_\phi \sigma_{r\phi}^2}{r} \\ &+ 2\rho \sigma_{r\phi}^2\frac{\partial u_\phi}{\partial r} + 2\rho \sigma_{z\phi}^2\frac{\partial u_\phi}{\partial z} \\ &+ 2\rho \sigma_{\phi\phi}^2\frac{1}{r}\frac{\partial u_\phi}{\partial \phi} = 0. \quad \text{(A7)}\end{aligned}$$

Off-diagonal elements of the velocity-dispersion tensor:

$$\begin{aligned}\frac{\partial}{\partial t}(\rho \sigma_{r\phi}^2) &+ \frac{1}{r}\frac{\partial}{\partial r}(r \cdot \rho \sigma_{r\phi}^2 \cdot u_r) + \frac{\partial}{\partial z}(\rho \sigma_{r\phi}^2 \cdot u_z) \\ &+ \frac{1}{r}\frac{\partial}{\partial \phi}(\rho \sigma_{r\phi}^2 \cdot u_\phi) + \frac{\rho \sigma_{r\phi}^2 u_r}{r} + \frac{\rho \sigma_{rr}^2 u_\phi}{r} \\ &- \frac{2\rho \sigma_{\phi\phi}^2 u_\phi}{r} + \rho \sigma_{rr}^2\frac{\partial u_\phi}{\partial r} + \rho \sigma_{r\phi}^2\frac{\partial u_r}{\partial r} \\ &+ \rho \sigma_{rz}^2\frac{\partial u_\phi}{\partial z} + \rho \sigma_{z\phi}^2\frac{\partial u_r}{\partial z} + \rho \sigma_{\phi\phi}^2\frac{1}{r}\frac{\partial u_r}{\partial \phi} \\ &+ \rho \sigma_{r\phi}^2\frac{1}{r}\frac{\partial u_\phi}{\partial \phi} = 0, \quad \text{(A8)}\end{aligned}$$

$$\begin{aligned}\frac{\partial}{\partial t}(\rho \sigma_{z\phi}^2) &+ \frac{1}{r}\frac{\partial}{\partial r}(r \cdot \rho \sigma_{z\phi}^2 \cdot u_r) + \frac{\partial}{\partial z}(\rho \sigma_{z\phi}^2 \cdot u_z) \\ &+ \frac{1}{r}\frac{\partial}{\partial \phi}(\rho \sigma_{z\phi}^2 \cdot u_\phi) + \frac{\rho \sigma_{z\phi}^2 u_r}{r} + \frac{\rho \sigma_{rz}^2 u_\phi}{r} \\ &+ \rho \sigma_{rz}^2\frac{\partial u_\phi}{\partial r} + \rho \sigma_{r\phi}^2\frac{\partial u_z}{\partial r} + \rho \sigma_{zz}^2\frac{\partial u_\phi}{\partial z} \\ &+ \rho \sigma_{z\phi}^2\frac{\partial u_z}{\partial z} + \rho \sigma_{\phi\phi}^2\frac{1}{r}\frac{\partial u_z}{\partial \phi} \\ &+ \rho \sigma_{z\phi}^2\frac{1}{r}\frac{\partial u_\phi}{\partial \phi} = 0, \quad \text{(A9)}\end{aligned}$$

$$\begin{aligned}\frac{\partial}{\partial t}(\rho \sigma_{rz}^2) &+ \frac{1}{r}\frac{\partial}{\partial r}(r \cdot \rho \sigma_{rz}^2 \cdot u_r) + \frac{\partial}{\partial z}(\rho \sigma_{rz}^2 \cdot u_z) \\ &+ \frac{1}{r}\frac{\partial}{\partial \phi}(\rho \sigma_{zr}^2 \cdot u_\phi) - \frac{2\rho \sigma_{z\phi}^2 u_\phi}{r} + \rho \sigma_{rr}^2\frac{\partial u_z}{\partial r} \\ &+ \rho \sigma_{zz}^2\frac{\partial u_r}{\partial z} + \rho \sigma_{rz}^2\frac{\partial u_z}{\partial z} + \rho \sigma_{r\phi}^2\frac{1}{r}\frac{\partial u_z}{\partial \phi} \\ &+ \rho \sigma_{z\phi}^2\frac{1}{r}\frac{\partial u_r}{\partial \phi} + \rho \sigma_{zr}^2\frac{\partial u_r}{\partial r} = 0. \quad \text{(A10)}\end{aligned}$$

Note that terms of third or higher order are neglected (zero-heat-flux approximation).

APPENDIX B: THE SIX COMPONENTS OF THE ARTIFICIAL VISCOSITY STRESS TENSOR *Q*

Here we give the components of the artificial viscosity stress tensor used in our simulations.

$$Q_{zz} = 2\mu_{\rm v}\left(\frac{\partial u_z}{\partial z} - \frac{1}{3}(\boldsymbol{\nabla} \cdot \boldsymbol{u})\right) \quad \text{(B1)}$$

$$Q_{zr} = \mu_{\rm v}\left(\frac{\partial u_z}{\partial r} + \frac{\partial u_r}{\partial z}\right) \quad \text{(B2)}$$

$$Q_{z\phi} = \mu_{\rm v}\left(\frac{\partial u_\phi}{\partial z} + \frac{1}{r}\frac{\partial u_z}{\partial \phi}\right) \quad \text{(B3)}$$

$$Q_{rr} = 2\mu_{\rm v}\left(\frac{\partial u_r}{\partial r} - \frac{1}{3}(\boldsymbol{\nabla} \cdot \boldsymbol{u})\right) \quad \text{(B4)}$$

$$Q_{r\phi} = \mu_{\rm v}\left(\frac{1}{r}\frac{\partial u_r}{\partial \phi} + \frac{\partial u_\phi}{\partial r} - \frac{u_\phi}{r}\right) \quad \text{(B5)}$$

$$Q_{\phi\phi} = 2\mu_{\rm v}\left(\frac{1}{r}\frac{\partial u_\phi}{\partial \phi} + \frac{u_r}{r} - \frac{1}{3}(\boldsymbol{\nabla}\cdot\boldsymbol{u})\right) \quad \text{(B6)}$$

APPENDIX C: TESTS AND ACCURACY

In this section we provide the results of two test problems probing the advection scheme and, especially, the conservation of the specific angular momentum. The results of other tests will be given elsewhere.

C1 Test 1: relaxation problem

The van Leer advection scheme was tested on a "relaxation" problem, in which a disk of constant density and velocity field proportional to r ($u_r = u_0 r$) is set, and the density is allowed to decrease. For this problem, the analytic solution of the continuity equation is $\Sigma(t) = \Sigma_0 e^{-2u_0 t}$ and it gives $\Sigma = 6.14 \times 10^{-6}\,\Sigma_0$ at $u_0 t = 6$. The numerical solution for this problem gives density values of $5.98 \times 10^{-6}\,\Sigma_0$ for the resolution of 256 radial grid points. When the density has decreased by nearly six orders of magnitude, its radial profile remains perfectly flat and the relative error is only 2.6%.

C2 Test 2: Conservation of specific angular momentum

An important point of concern when numerically studying the dynamics of galaxies is the ability of a code to conserve specific angular momentum. A comprehensive test problem on specific angular momentum conservation that covers advection as well as pressure and gravity terms in the momentum equations was designed by Norman et al. (1980). These authors considered the isothermal gravitational collapse of rotating axisymmetric prestellar clouds in cylindrical geometry. For a fluid with no mechanism for redistributing angular momentum, the mass $M(K)$ in the cloud with specific angular momentum $K = \Omega r^2$ less than or equal to K is a constant of motion. Deviations from the initial spectrum $M(K)$ reveal a redistribution of angular momentum. We consider a similar test problem of isothermal gravitational collapse of a flattened axisymmetric prestellar cloud (further referred as a "disk") that can be studied in the thin-disk approximation (see e.g. Basu 1997). This problem should test the ability of our polytropic model (for which we set $\gamma = 1$ to switch to the isothermal regime) to conserve the specific angular momentum. For a uniformly rotating gas disk ($\Omega = \Omega_0$) with the radial surface density distribution given by Basu (1997),

$$\Sigma(r) = \frac{r_0 \Sigma_0}{\sqrt{r^2 + r_0^2}}, \quad \text{(C1)}$$

the initial specific angular momentum spectrum is

$$M(K) = 2\pi\Sigma_0 r_0^2 \left(\sqrt{1 + \frac{K}{K_0}} - 1\right), \quad \text{(C2)}$$

where $K_0 = \Omega_0 r_0^2$, Σ_0 is the central surface density, and $r_0 = c_{\rm s}^2/(1.5G\Sigma_0)$ is the characteristic scale length which is comparable to the Jeans length $\lambda_{\rm J} = c_{\rm s}^2/(G\Sigma)$ of a non-rotating cloud. We choose $\Sigma_0 = 3.55 \times 10^{-2}$ gm cm^{-2}, $c_{\rm s} = 0.188$ km s^{-1} (equivalent to $T = 10$ K), $\Omega_0 = 0.4$ km s^{-1} pc^{-1}, and the mean molecular weight 2.33 (molecular hydrogen with a 10% admixture of atomic helium). The disk has the inner and outer radii of $r_{\rm in} = 10$ AU and $r_{\rm out} = 20000$ AU. We introduce a "sink cell" at $r < 10$ AU and impose a free inflow inner boundary condition and a constant mass and volume outer boundary condition. The mass of our disk is 2.45 $M_\odot$.

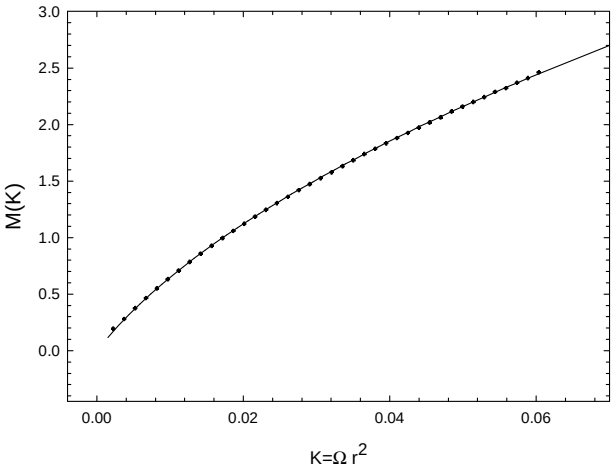

Figure C1. The specific angular momentum spectrum of a collapsing flattened cloud. The quantity $M(K)$ is the total mass in the cloud with specific angular momentum less than or equal to $K = \Omega r^2$. The solid line shows the theoretical spectrum at $t = 0$ yr. The filled circles gives $M(K)$ at 0.185 Myr after the beginning of the simulation when the central protostar has already formed. A good agreement between both spectra indicates virtually no angular momentum redistribution, as is indeed expected for the axisymmteric collapse.

The ratios of rotational and thermal energies to the gravitational energy of the initial configuration are 0.7% and 25%, respectively. The disk is thus gravitationally unstable and is allowed to collapse under its own gravity. The initial theoretical spectrum $M(K)$ is shown in Fig. C1 by the solid line. The early evolution is characterised by a slow gravitational contraction and a subsequent runaway collapse. When the density in the sink cell exceeds 13.3 g cm^{-2}, the central protostar is assumed to form (due to a transition to the adiabatic phase). The filled circles plot $M(K)$ computed at $t = 4300$ yr after the formation of the central protostar (0.185 Myr after the beginning of the simulation). At this time, approximately 0.3 $M_\odot$ has been accreted by the protostar. As is clearly seen, $M(K)$ merges with the initial spectrum (except for the end points where a minimal deviation is observed), indicating virtually no angular momentum redistribution due to either physical or numerical reasons. This is expected in the axisymmetric collapse with very little numerical diffusion.